Surface-enhanced Raman Spectroscopy Facilitates the Detection of Microplastics < 1 μm in the Environment

Guanjun Xu[1], Hanyun Cheng[1], Robin Jones[2], Yiqing Feng[1], Kedong Gong[1], Kejian Li[1], Xiaozhong Fang[1], Muhammad Ali Tahir[1], Ventsislav Kolev Valev[2], Liwu Zhang[1,3]*

[1]Shanghai Key Laboratory of Atmospheric Particle Pollution and Prevention, Department of Environmental Science & Engineering, Fudan University, Shanghai, 200433, Peoples' Republic of China

[2]Centre for Photonics and Photonic Materials and Centre for Nanoscience and Nanotechnology, Department of Physics, University of Bath, Claverton Down, Bath BA2 7AY, United Kingdom

[3]Shanghai Institute of Pollution Control and Ecological Security, Shanghai, 200092, Peoples' Republic of China.

ABSTRACT: Micro- and nanoplastics are considered one of the top pollutants that threaten the environment, aquatic life and mammalian (including human) health. Unfortunately, the development of uncomplicated but reliable analytical methods that are sensitive to individual microplastic particles, with sizes smaller than 1 μm, remains incomplete. Here, we demonstrate the detection and identification of (single) micro- and nanoplastics, by using surface-enhanced Raman spectroscopy (SERS), with Klarite substrates. Klarite is an exceptional SERS substrate; it is shaped as a dense grid of inverted pyramidal cavities, made of gold. Numerical simulations demonstrate that these cavities (or pits) strongly focus incident light into intense hotspots. We show that Klarite has the potential to facilitate the detection and identification of synthesized and atmospheric/aquatic microplastic (single) particles, with sizes down to 360 nm. We find enhancement factors of up to two orders of magnitude for polystyrene analytes. In addition, we detect and identify microplastics with sizes down to 450 nm on Klarite, with samples extracted from ambient, airborne particles. Moreover, we demonstrate Raman mapping as a fast detection technique for sub-micron microplastic particles. The results show that SERS with Klarite is a facile technique that has the potential to detect and systematically measure nanoplastics in the environment. This research is an important step towards detecting nanoscale plastic particles that may cause toxic effects to mammalian and aquatic life when present in high concentrations.

KEYWORDS: SERS; microplastics; Raman mapping; Klarite; nanoplastics

1. INTRODUCTION

The abundance of microplastics has become one of the most concerning environmental issues in the modern world and has attracted widespread research interest.[1] In the last five years alone, microplastics in fresh water,[2-7] seawater,[8, 9] sediments and beach sand [10, 11] have become the subject of intense research. Some of these studies have reported atmospheric microplastics in megacities such as Paris[12] and Shanghai,[13] as well as in large cities, such as Dongguan [14] and Hamburg. [15] A recent study has even reported the transport and deposition of these microplastics in a remote, pristine mountain catchment (French Pyrenees). [16]

Due to their small size, low density and resistance to biodegradation,[17, 18] microplastics can survive in the environment for centuries, contributing to microbiota dysbiosis and inflammation in aquatic organisms, such as intertidal fish and zebrafish.[19, 20] Plastics with enriched organic pollutants and trace metals may contaminate food chains, transferring along an arterial food chain from algae through zooplankton to fish and tend to aggregate in higher trophic level species, occurring in commercial food, sometimes ending with human consumption.[21-27] Microplastics decay further through mechanical abrasion, photodegradation and biodegradation, forming nanoplastics that can pass through biological membranes and readily translocate between different tissues.[28] These nanoplastics have significantly more potent toxicological properties,[29, 30] because they can enter animal cells and cross the epithelial tissues; if inhaled, airborne nanoplastics can even cross the pulmonary epithelial lining.[31, 32]

There are various techniques for the detection of atmospheric particles such as aerosol-time-of-flight mass spectrometry (ATOFMS),[33] single-particle aerosol mass spectrometry (SPAMS), [34] atomic force microscopy (AFM),[35] Fourier transform infrared spectroscopy (FTIR),[36] transmission and scanning electron microscopy (TEM and SEM),[37, 38] Raman spectroscopy combined with electrodynamic balance (EDB). Owing to the required detection resolution, [39, 40] Raman spectroscopy has been used to detect microfibers in surface water and microplastics in ambient atmosphere.[41, 42] Gillibert et al.[43] have demonstrated single microplastic particle detection and identification with sub-20 μm particle sizes (down to the 50 nm range) using optical trapping tweezers combined with Raman spectroscopy.

However, standard Raman instruments are the most commonly available and are inherently limited to ensemble detection of microplastics. The detection of single microplastic particle < 1 μm with traditional Raman spectroscopy techniques is rather difficult due to the weak Raman signal. Given that these nanoplastics have significant toxicity potential and can readily cross pulmonary epithelial tissues,[32] a facile method for detecting and identifying nanoplastic particles is urgently needed.

Surfaced-enhanced Raman spectroscopy (SERS) provides a facile and rapid method to obtain chemical information on particles. Single particles situated in the "hotspots" can attain large enhanced factors (up to 6 orders of magnitude) due to electromagnetic field enhancement effects,[44] and, for some molecules, the SERS enhancement is truly huge (8 to 11 orders of magnitude), due to plasmonic charge transfer effects. [45] So far, SERS has been applied to study atmospheric fine particles and secondary organic aerosol particles.[44, 46] To the best of our knowledge, no SERS research has been reported on single microplastics < 1μm.

In this work, the detection of single nanoplastics is enabled by the use of Klarite – a commercial SERS substrate. It has an ordered, dense grid structure of cavities (or "pits") that are shaped as inverted pyramids. Each pit structure is 1.5 μm wide, making Klarite highly suitable for studying nanoparticles.[40] SERS of both polystyrene (PS) and polymethyl methacrylate (PMMA) spheres are compared on both Klarite and silicon wafer. To further demonstrate the real-world application of the technique, ambient atmospheric micro-nanoplastic samples are collected and tested.

2. EXPERIMENTAL SECTION

2.1. Polystyrene and Polymethyl Methacrylate Spheres

PS spheres with diameters of 360 nm, 500 nm, 1μm, 2 μm and 5 μm and PMMA spheres with diameters 360 nm, 500 nm, 2 μm, 5 μm (supplied as 10% (w/v) mono-dispersed in deionized water) were purchased from Shanghai Huge Biotech Co, China (Figure S1). The mass density of the PS material is 1.05 g/cm^3. Both PS and PMMA Particles were diluted with deionized water to a ratio of 1:4×10^4 with the volume of 4 ml in order to access individual particles. The final concentration of the plastic particles is 2.625×10^{-5} g/cm^{-3}.

2.2. Ambient atmospheric aerosol particles

The Intelligent Total Suspended Particulate (TSP) Comprehensive Sampler (Laoying Environmental Technology Co, China) was employed to sample atmospheric microplastic particles (Figure S2). Ambient atmospheric aerosol particles were sampled on the roof of the building of the department of environmental science and technology, Fudan University (121°30'E, 31°20′N) from 11th November 2019 to 17th November 2019. Moreover, 90 mm quartz microfiber filters (Whatman) were used for sampling. The sampled particles with size < 2.5 μm were collected in clean aluminum film for the following steps. To reduce interference in Raman spectra from organic, biogenic and other non-plastic matter that could be present in the sampled particles, the particles were rinsed in a glass container with hydrogen peroxide (H_2O_2) solution (30%) for 24 hours at room temperature, and the glass bottles were covered with clean glass all the time to avoid contamination. The solution was then filtered with a 47 mm diameter glass fiber filter (Whatman) and rinsed with deionized water. Finally, the solution was concentrated by heating to 60 °C in a clean glass container for 24 hours and transferred to Klarite substrates using a glass pipette.[47] During the experiment, lab blanks and field blanks were collected. In order to avoid interferences from the sampling equipment and the lab, the sampler was washed by deionized water after each sampling, the quartz membranes after sampling were collected in clean aluminum foil. In addition, the sample were prepared whilst wearing cotton lab coats, using glass pipettes instead of plastics droppers and the beaker was covered with a piece of glass during the dilution process.

2.3. Raman microspectroscopy

Raman spectroscopy was performed with an XploRA Plus confocal Raman spectrometer (Jobin Yvon, Horiba Gr, France) coupled with a ×100 Olympus microscope objective (Olympus, 0.90 Numerical Aperture). The sample was excited by an external-cavity diode laser (785 nm), operating at power of 25 mW. The diffraction grating density had 1200 lines per mm, the blaze wavelength is 750 nm. Spectra were collected using a multichannel EMCCD device with the confocal imaging of 0.5 μm XY, the resolution of 1.4 cm^{-1} full width at half maxima. The spectra were collected from 200 cm^{-1} to 2000 cm^{-1}, with 15 spectra accumulations for the lab-generated sample and 50 spectra accumulations for the ambient atmospheric aerosol sample at 5 s acquisition time per spectrum. Raman mapping was performed using point by point scanning mode with a 1 μm step size.

2.4 Data processing

To analyze the data, baseline removal was performed in Labspec 6 software by a polynomial equation which best fits the background of the spectrum. The peak wavenumber and intensity were analyzed using Gauss-Lorenz Gauss fit.

2.5 Numerical simulations

Finite difference time domain (FDTD) simulations were performed in Lumerical (a commercially available photonic simulation software) to gain insight into the electric-field distribution within the inverted pyramidal pits of the Klarite substrates. The material properties of the Au Klarite substrate was emulated using a Johnson & Christy model for Gold. Nine pyramidal pits were generated in the design modeller in a 3 x 3 grid with dimensional equality to the experimental Klarite. The Eulerian mesh was a cuboid FDTD simulation domain enclosing the central pit (a single unit cell). The granularity of the mesh was 8.5 nm and was selected based on a mesh sensitivity study to determine convergence and quality of results (see Supplemental section Figure S3). In the Cartesian basis, the z direction is normal to the surface of the Klarite; the x and y directions coincide with the plane of the Klarite surface. Periodic boundary conditions were applied in the x and y directions; simulating an infinite array of pyramidal pits. A perfectly matched layer (PML) boundary condition was applied to the upper and lower boundaries of the domain to model an open boundary.

A linearly polarised plane wave pulse of light was incident directly onto the Klarite from 0.7 μm above the surface. The spectrum of the pulse was nominally centred at 785 nm to match the experimental laser wavelength of this study and had a bandwidth of 500 nm; the amplitude of the pulse was E_0= 0.5 V/m. A planar electric field monitor was placed in the vertical cross-section of the inverted pyramid pit, perpendicular to the direction of polarisation to extract the plasmonic electric field distribution at the wavelength of the incident light. The simulations were repeated for two other wavelengths of incident light (685 nm and 885 nm) to determine the wavelength dependence of the electric field distribution.

2.6 Klarite, Raman, and plastic particle setup

For sample preparation, 100 μL of microplastic sample solution containing PS, PMMA or ambient sample was dropped onto the Klarite using a glass pipette and then dried at room

158 temperature. The Klarite is fixed on a glass slide, therefore it can be put on the stage of the
159 XploRA Plus confocal Raman spectrometer. A photo of the setup is provided in the
160 supporting information (Figure S2). Environmental samples are usually more complicated
161 and often fluoresce.[48] Compared with visible light such as 532 nm and 633 nm, 785 nm laser
162 wavelength can avoid the fluorescence effectively.
163

164 **3. RESULTS AND DISCUSSION**

165 **3.1. Standard Raman and SERS detection of PS particles**

166 Raman spectra are collected from PS particles with 5 different sizes, ranging from 360 nm
167 to 5 μm. The particles are placed on silicon wafers (a standard non-SERS substrate) and on
168 Klarite (commercial SERS substrate). Figure 1a shows the Raman spectra of PS spheres on a
169 silicon wafer. Figure 1b-f show the corresponding optical images (bright field microscopy, in
170 reflection) of the PS spheres. Clearly, signal from the PS spheres is hardly detectable; the
171 characteristic Raman spectrum of silicon dominates the signal. [49] Only the 5 μm PS spheres
172 show a prominent peak at 1003 cm^{-1}, with intensity less than 1000. The smaller PS particles
173 on the silicon wafer only exhibit strong peaks at 521 cm^{-1} and 800~1000 cm^{-1}, which is the
174 Raman signal of the Silicon. The appearance of the Silicon substrate signal is due to the larger
175 laser spot size of the confocal Raman spectrometer compared with the PS particle size.
176 By contrast to Si, Figure 2 shows the Raman spectra, optical microscopy images and SEM
177 images of PS spheres on Klarite substrates (see Supplemental section Figure S4). PS spheres
178 with sizes of 2 μm and 5 μm can be directly observed and studied under the optical
179 microscope that is integrated with our Raman spectrometer, as shown in Figure 2c and 2d.
180 Single PS spheres with sizes smaller than 1 μm become difficult to observe and identify
181 under the optical microscope (see Supplemental section Figure S5). The ordered structure of
182 Klarite provides the means of indexing the location of every pyramidal pit under SEM and
183 optical microscopy. Hence, PS spheres that cannot be distinguished under the optical
184 microscope can still be mapped out, using SEM, allowing their Raman spectra to be studied
185 by locating their indexed pyramidal pit. Figure 2e and 2f present SEM images of individual
186 PS spheres of size 360 nm and 500 nm in their indexed inverted pyramidal pits.

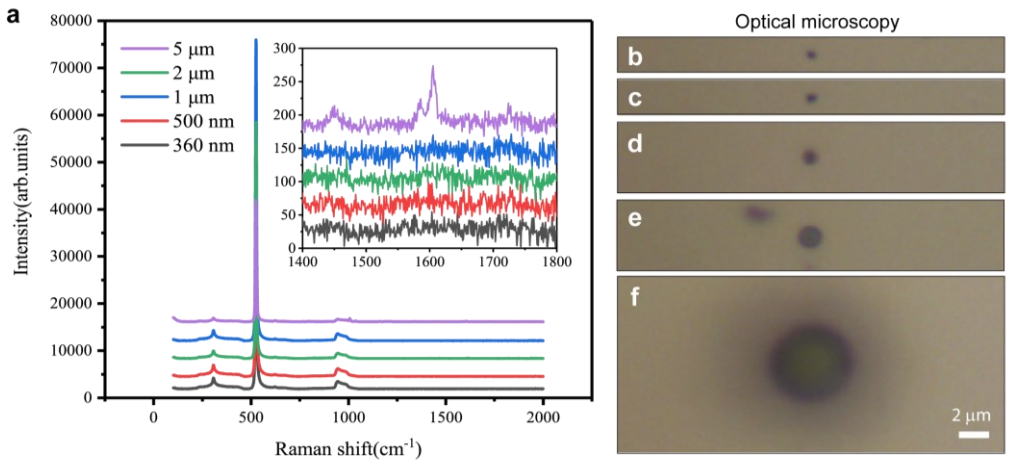

Figure 1. (a) Raman spectra of polystyrene (PS) spheres of variable size on silicon wafers (5 × 15 second spectral acquisitions) (Inset: spectra from 1400 to 1800 cm^{-1}). (b - f) Optical, bright field microscopy images, in reflection, of 360 nm (b); 500 nm (c); 1 µm (d); 2 µm (e); 5 µm (f) PS particles, placed on silicon wafers. Scale bars: 2 µm.

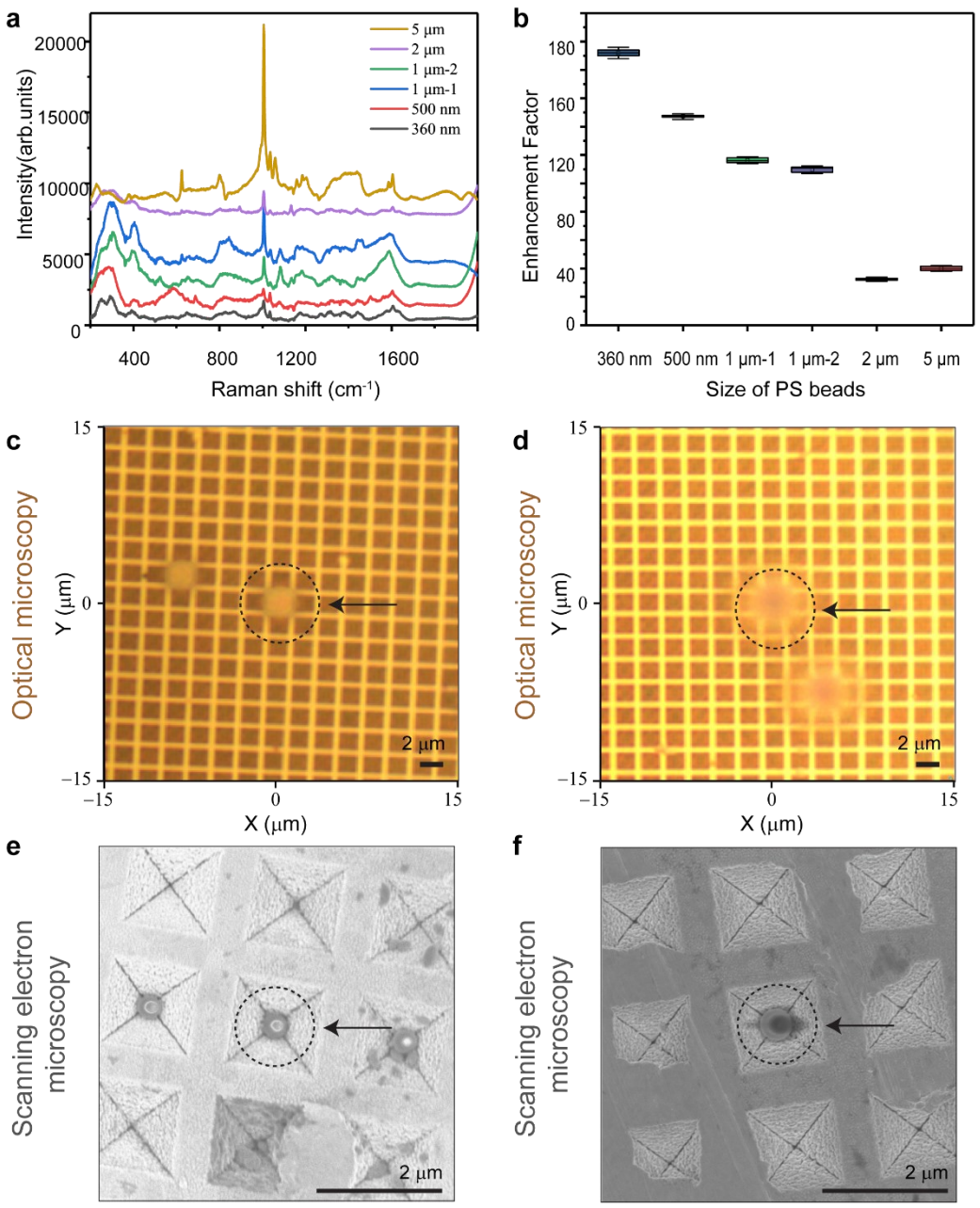

193

194 **Figure 2.** (a) Raman spectra of polystyrene (PS) spheres of variable size deposited on Klarite
195 substrates (5 × 15 second spectral acquisitions). (b) Box and whisker plot of enhancement
196 factors (EF) of PS particles as a function of size. (c, d) Optical, bright field microscopy
197 images of 2 µm (c) and 5 µm (d) PS spheres on Klarite. (e, f) Scanning electron microscopy
198 (SEM) image of 360 nm (e) and 500 nm (f) PS spheres on Klarite. Images of other size are
199 shown in Figure S4-S5. Scale bars: 2 µm.

200 Figure 2a and 2b present the Raman spectra of PS particles located through the Klarite pit

indexing method. The Raman signal of single PS particles (as small as 360 nm in diameter) are clearly detectable (Figure 2a). The two most prominent peaks at 1003 cm^{-1} and at 1033 cm^{-1} are attributed to the ring-mode vibrations of a monosubstituted aromatic compound (ν(C-C) and β (C-H)) in PS.[37] Hence, in sharp contrast to the samples on silicon wafers, PS particles smaller than 5 μm can clearly be identified in Raman spectra on Klarite substrates. This identification illustrates the powerful potential of Klarite to enhance the Raman signal intensity in samples with weak Raman scattering signals. The 500 nm PS spheres also exhibit significant Raman peaks in the aforementioned regions, although the peak intensity is not as strong as that of the 360 nm PS spheres on Klarite. Both the 1 μm and 5 μm PS spheres on Klarite show much stronger intensities relative to that on silicon wafers (Figures 1a and 2a).

The location of the PS spheres on Klarite is critical to the signal strength. Figure 2a presents Raman spectra for PS spheres inside and outside of the inverted pyramidal cavities, labelled as 1 μm-1 and 1 μm-2 respectively. For 1 μm PS spheres located outside of the pyramidal pits, the Raman peak intensity is lower than that of PS spheres with same size located inside of the pits. Likewise, the 2 μm PS spheres show a lower peak intensity than that of the 1 μm-1 spheres. It is reasonable to assume that these 2 μm particles are simply too large to fit well into the pyramidal pits (which are 1.5 μm wide) and, therefore, do not benefit from the electric field enhancement as significantly.

Since the peaks of PS overlap with the signal of Silicon substrate, we have also studied the Raman spectra of PS on different substrates such as glass and Al foil, which show flat background for Raman measurement. The results were shown in Figure S6 to S8. Glass slide shows flat background under 532 nm laser wavelength, while shows broad background peak at 1100-1600 cm^{-1} under 785 nm laser. In both cases, hardly any characteristic peaks of PS can be observed when the size is smaller than 1μm, confirming the superiority of Klarite substrate. Al foil is also a good substrate for comparison, which is smooth and flat, showing almost no interference signals (Figure S9). Compared with Al foil, Klarite (the signal of Klarite without particles is shown in Figure S10) shows an EF of 1091.96 for PS of 360 nm, further confirming the results obtained on Silicon substrate.

Figure 3 presents the simulated plasmonic electric-field distribution within the pyramidal pits of the Klarite, at illumination wavelengths 685 nm, 785 nm and 885 nm. We have

231 previously demonstrated that the hotspot pattern evolves with wavelength; [50] here, the figure
232 shows that whereas a complex hotspot pattern is present at 685 nm, at 785 nm and at 875 nm
233 the field is mostly concentrated in the lower portion of the pit. These data demonstrate that
234 the most significant SERS can be expected from Raman active analytes situated in the lower
235 portion of the pit. It follows that the SERS enhancement is strongly dependent on the particle
236 size relative to the Klarite pit size. Further on, the manufactured Klarite pit size could be
237 adjusted to suite a particular particle size. Although such size adjustments would affect the
238 plasmon resonance wavelength, Figure 3 shows that the main hotspot in the lower part of the
239 pit is spectrally quite broad (small maximum intensity changes over a 200 nm range).
240 It should be noted that nanoscale texture can provide enhancement, and achieve the goal of
241 probing molecules. Gold thickness and pit angle can influence the SERS enhancement. It has
242 also been established that in a standard Klarite pit, it is diffraction that contributes to the
243 enhanced SERS signal, and the plasmon effect will only become noticeable by decreasing the
244 gold film thickness. [51] In our study, the size of the microplastic is much larger than that of the
245 gold nanoparticles. These plastic particles can hardly get into the “hotspot” of nanoscale
246 structure. Therefore, the enhancement is mainly attributed to electric field enhancement
247 increased by the pyramid pits that the particles fall into.
248
249

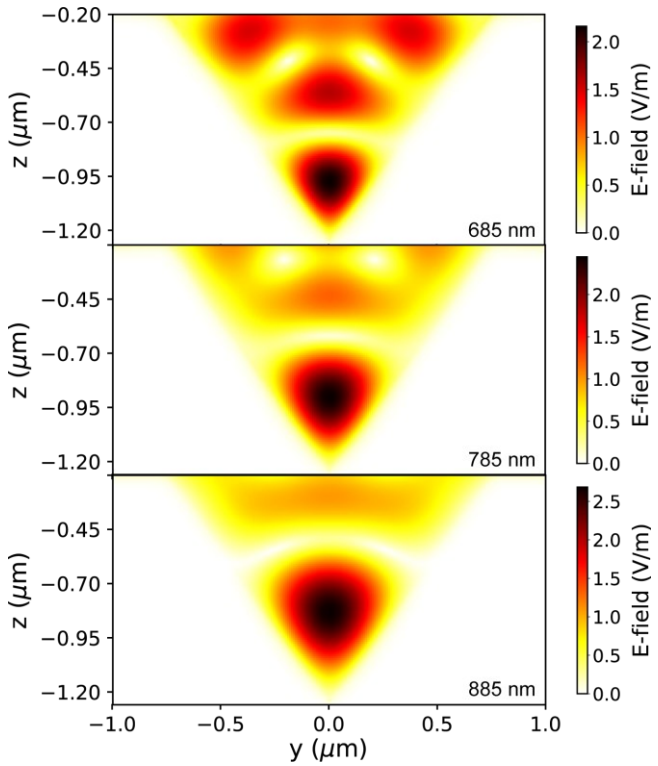

Figure 3. Klarite strongly focusses the electric field (E-field) of light within the pit volume, for a broad range of wavelengths around our laser wavelength (785 nm). Three numerical simulations of the E-field distribution show clear hotspot patterns. The simulations were performed for illumination at 685 nm, 785 nm and 885 nm.

3.2. Enhancement Factor of Klarite Samples

We quantify the enhancement factors (EF) of the SERS according to the following equation:

$$EF = \frac{I_{SERS}/N_{SERS}}{I_{NRS}/N_{NRS}}, \quad (1)$$

where I_{SERS} and I_{NRS} are defined as peak intensities detected by the SERS substrate and non-SERS substrate respectively; N_{SERS} and N_{NRS} refer to the number of molecules that contribute to the intensity of SERS and non-SERS Raman peak intensities respectively. [47] In this research, we measure a single particle situated in the pit mapped by SEM, therefore N_{SERS} and N_{NRS} is fixed as N=1. Hence, we compute the EF for single particles with consistent sizes to quantify the EF as a function of particle size. The accumulation time and laser power were kept constant to eliminate their influence on the measured Raman intensity.

In addition, all samples were prepared with consistent concentrations of PS spheres. Hence, the number of contributing particles (N_{SERS} and N_{NRS}) for a given particle size was considered to be constant between SERS and non-SERS samples. The Raman intensity peak height was measured after removing the baseline spectrum of the substrate.

Figure 2b presents the calculated EFs of the Raman signal at a shift of 1600 cm^{-1} for PS particles as a function of size. Three particles of each size are selected randomly and measured five times to avoid the influence of fluctuation and make sure the signal is stable and available for further research. One of the spectra is randomly chosen to represent the signal (very similar). The average EF and standard deviation for PS spheres with 360 nm diameter is 172 (±22), while the highest value is 176.03. The average EF for the 500 nm PS spheres is 127 (±1), which is a slight decline relative to that of the 360 nm spheres. The EF of 1 μm PS spheres also show a slight decline relative to the 500 nm PS spheres, with the average value of 97 (±2) and a maximum value of 98.80. The EF of 5 μm PS spheres is 20 (±2). Compared with particles located within in the pyramidal pits, particles on the top surface of the Klarite show a relatively low EF. For example, the average EF of 1 μm PS spheres outside of the pyramidal pits (labelled 1 μm-2) and 2 μm PS spheres are 90 (±2) and 12 (±1), respectively. For the 5 μm PS spheres, although the SERS peak intensity is the strongest of all particle sizes, the EF value is not as significant as that of the 360 nm PS sphere, indicating that the peak intensity has both a strong particle size and particle location dependence.

The intensities in our experiments are an order of magnitude greater than previously reported for microplastics by Raman spectra; [43] however, there are differences in the test conditions. Our results highlight the potential of Klarite to enhance Raman scattering for SERS with trace amounts of small particles that are otherwise undetectable using standard Raman microscopy. In tandem with SEM imaging, individual 360 nm PS spheres are successfully identified, located and measured using SERS. To the best of our knowledge, in the microplastic research field, these are the smallest individual nanoplastic particles measured to date, with SERS.

3.3. SERS detection of PMMA particles of different size

In order to further test the versatility of Klarite for SERS detection and identification of

296 microplastics, PMMA was also investigated. PMMA is commonly used as a substitute for
297 glass and can be made into a wide range of products ranging from aircraft canopies to
298 dentures and trays. For reference, Figure 4 shows Raman spectra (a) and optical images (b-e)
299 of PMMA spheres on silicon wafers. As with PS, the Raman spectra of PMMA on silicon
300 wafers (Figure 4a) are dominated by the characteristic Raman spectrum of the silicon
301 substrate. The characteristic peak of PMMA at 1453 cm^{-1} is observed only on 5 μm PMMA
302 spheres. The Raman spectra of PMMA on Al foil substrate is also studied and shown in
303 Figure S9.
304 Figure 5a shows the Raman spectra of PMMA spheres on Klarite. The peaks at 622 cm^{-1},
305 817 cm^{-1}, 1000 cm^{-1}, 1200 cm^{-1}, 1452 cm^{-1} and 1723 cm^{-1} are clearly visible and attributed to
306 C-C-O stretching, C-O-C symmetric stretching, C-C stretching, C-H bending and C=O
307 stretching, respectively. To avoid interference from Si, peak at 1452 cm^{-1} was chosen for the
308 subsequent Raman mapping and EF calculations. In Figure 5b, the box and whisker plot of
309 EF as a function of particle size are shown. The 360 nm PMMA particles exhibit the strongest
310 peak intensity, with EFs ranging from 23 to 30. The EF of 500 nm PMMA spheres show a
311 slight decline relative to that of 360 nm PMMA spheres, ranging from 11 to 15; while the EF
312 of 5 μm PMMA spheres ranging from 5 to 8. The 2 μm PMMA spheres give the smallest EF,
313 ranging from 2 to 4. For visualization, in Figure 5c-d, the optical, bright field microscopy
314 images of the PMMA spheres with size 2 μm and 5 μm are presented. Similarly, SEM images
315 are displayed in Figure 5e and 5f, for PMMA spheres with size 360 nm and 500 nm,
316 respectively.
317 Comparison of Figures 2b and 5b clearly shows that the EF of PMMA is significantly less
318 than PS, it has also been reported that longer acquisition time is required for PMMA study in
319 order to get the same signal intensity of PS. [43] According to the Kramers-Heisenberg-Dirac
320 scattering formula, Raman signal can be enhanced by resonant Raman signal, while lower
321 Raman cross section and low sensitivity to substrate may lead to the SERS reduced. [52] We
322 suggest the lower EF of PMMA is due to the low normal Raman cross section and low
323 sensitivity to the Klarite substrate.
324

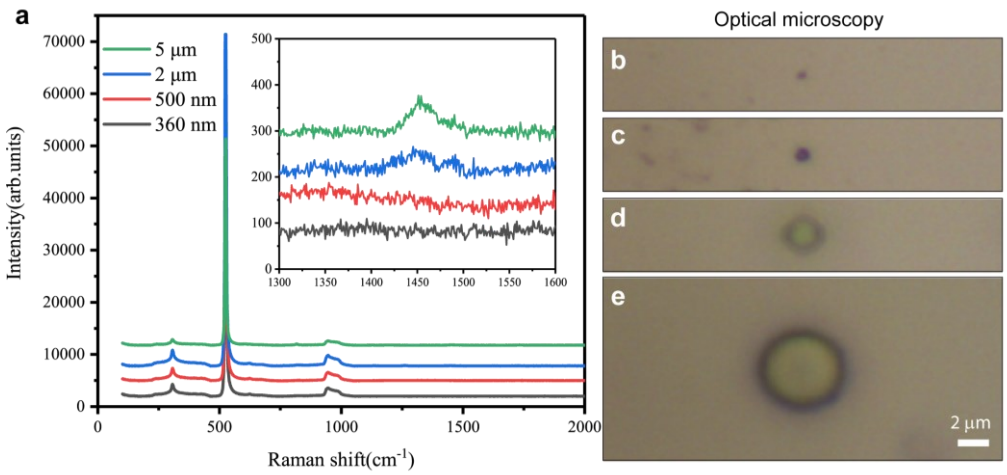

325

326 **Figure 4.** (a) Raman spectra of polymethyl methacrylate (PMMA) spheres of variable size on

327 silicon wafers (5 × 15 second spectral acquisitions). (b – e) optical, bright field microscopy

328 images of 360 nm (b); 500 nm (c); 2 µm (d); 5 µm (e) PMMA particles on silicon wafers.

329 Scale bars: 2 µm.

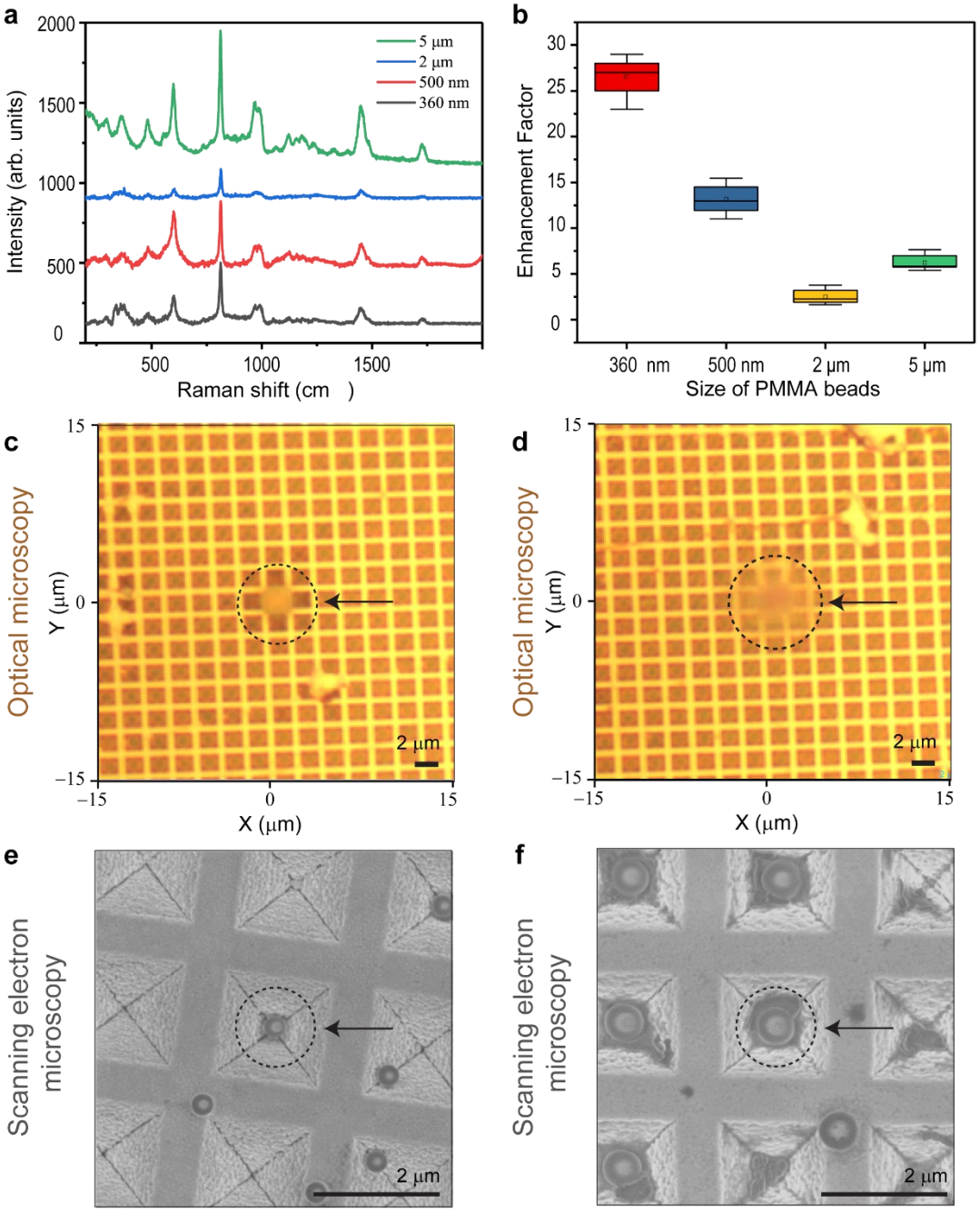

330

331 **Figure 5.** (a) Raman spectra of polymethyl methacrylate (PMMA) spheres of variable size
332 deposited on Klarite substrates (5 × 15 second spectral acquisitions). (b) Box and whisker
333 plot of enhancement factors (EF) of PMMA particles as a function of size. (c, d) Optical
334 images of 2 µm (c) and 5 µm (d) PMMA spheres on Klarite. (e, f) Scanning electron
335 microscopy (SEM) images of 360 nm (e) and 500 nm (f) PMMA spheres on Klarite. Scale
336 bar: 2 µm.

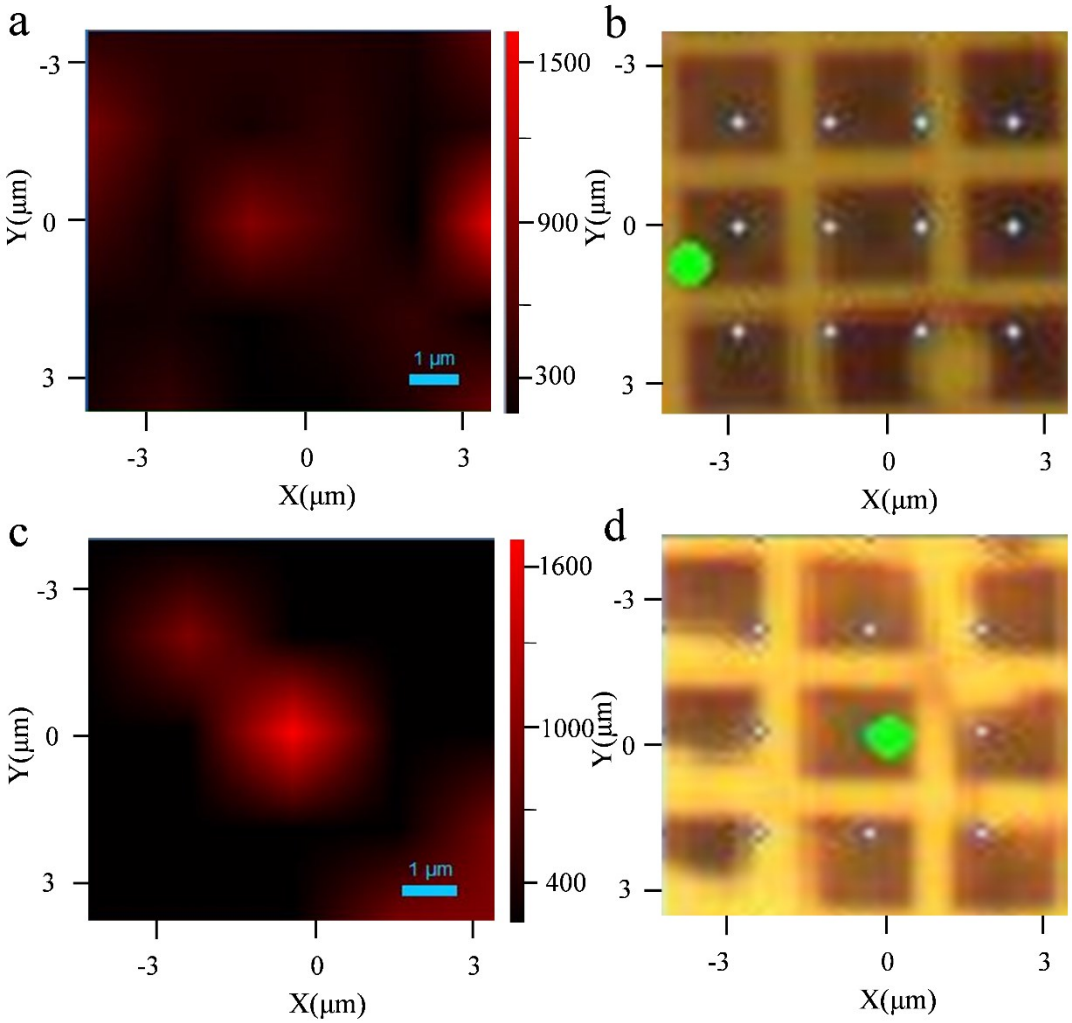

Figure 6. (a, b) Raman mapping image (a) and optical, bright field microscopic image (b) of 360 nm polystyrene (PS) spheres on Klarite. (c, d) Raman mapping image (c) and optical, bright field microscopic image (d) of 500 nm PMMA spheres on Klarite. Scale bars: 1 μm. In (a) and (c), the red-scale of the false-color image represents the intensity change of Raman peaks. The green spot in b and d is the laser focus point while white spots are the sampling points.

3.4. Raman Mapping with SERS

In the absence of SEM techniques, SERS with Raman mapping can be used to detect microplastics smaller than 1 μm. Figure 6 shows Raman maps of PS and PMMA spheres with sizes of 360 nm and 500 nm, respectively, on Klarite. The mapped region is about 7.5×7.5

μm^2, and was mapped with a step size of 1.5 μm. The prominent peak of PS at 1003 cm^{-1} was selected as the mapped spectral filter. The peak of PMMA at 1452 cm^{-1} was selected as the mapped spectral filter. The red-scale of the false-color image represents the intensity change of Raman peaks. As illustrated in Figure 6a and 6c, the distribution of nano PS and PMMA spheres on Klarite substrates are clearly shown, confirming that Raman mapping can be applied to identify nanoplastics with SERS.

3.5. SERS of atmospheric samples extracted from the air in Shanghai

Ambient atmospheric microplastics were extracted on the roof of the building of the department of environmental science and technology, at Fudan University and treated as detailed in the experimental section prior to deposition onto Klarite substrates. Figure 7 shows spectra from selected particles extracted in Shanghai on Klarite. The spectra in the upper panels of Figure 7a and 7b were found to match polyethylene terephthalate (PET) and PS reference standard spectra, shown in the corresponding lower panels (SEM images are shown in Figure S11). The detection of PET further certify that Klarite is a promising substrate in detecting various microplastics in environment. The PET particle exhibits a Raman peak at 633cm^{-1}, which corresponds to the vibration of aromatic C=C in plane ring deformation and a peak at 858 cm^{-1} which corresponds to the vibration of aromatic C=C out of plane deformation. The PET Raman peak at 1300 cm^{-1} is associated with the CH_2 twisting vibration and the vibration of aromatic in plane CH deformation. There are also peaks at 1620 cm^{-1} and 1760 cm^{-1}, which are attributed to the C-O stretching and C=O stretching vibration, respectively. The Raman spectra from particles identified as PS exhibit Raman peaks comparable with those presented in Figure 6 (Section 3.4).

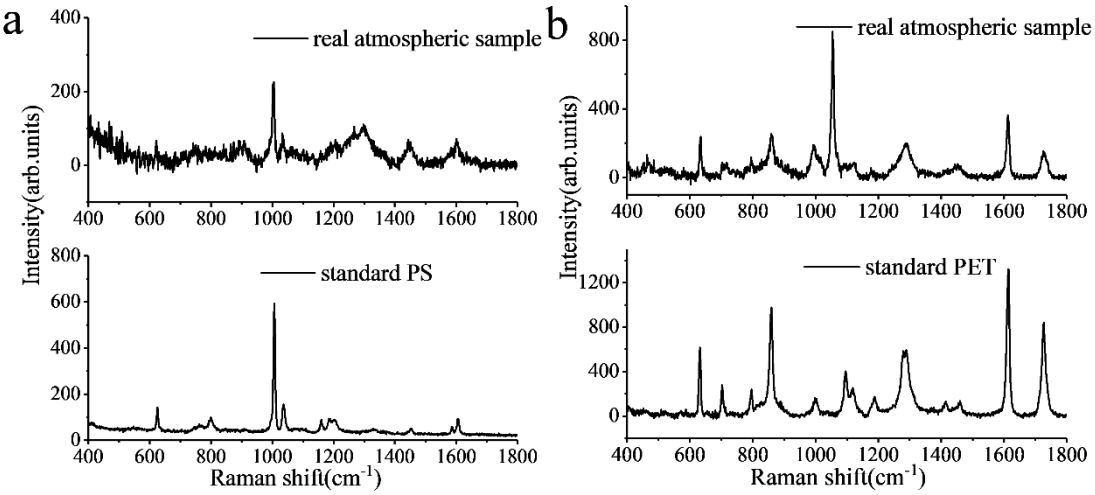

372

373 **Figure 7.** (a, top) Raman spectra of particles identified as polyethylene terephthalate (PET)
374 from atmospheric samples extracted in Shanghai (5 × 50 second spectral acquisitions). (b, top)
375 Raman spectra of particles identified as polymethyl methacrylate (PMMA) particles from
376 atmospheric samples extracted in Shanghai (5 × 50 second spectral acquisitions). (a and b,
377 bottom) corresponding reference standard spectra for PET and PMMA respectively.

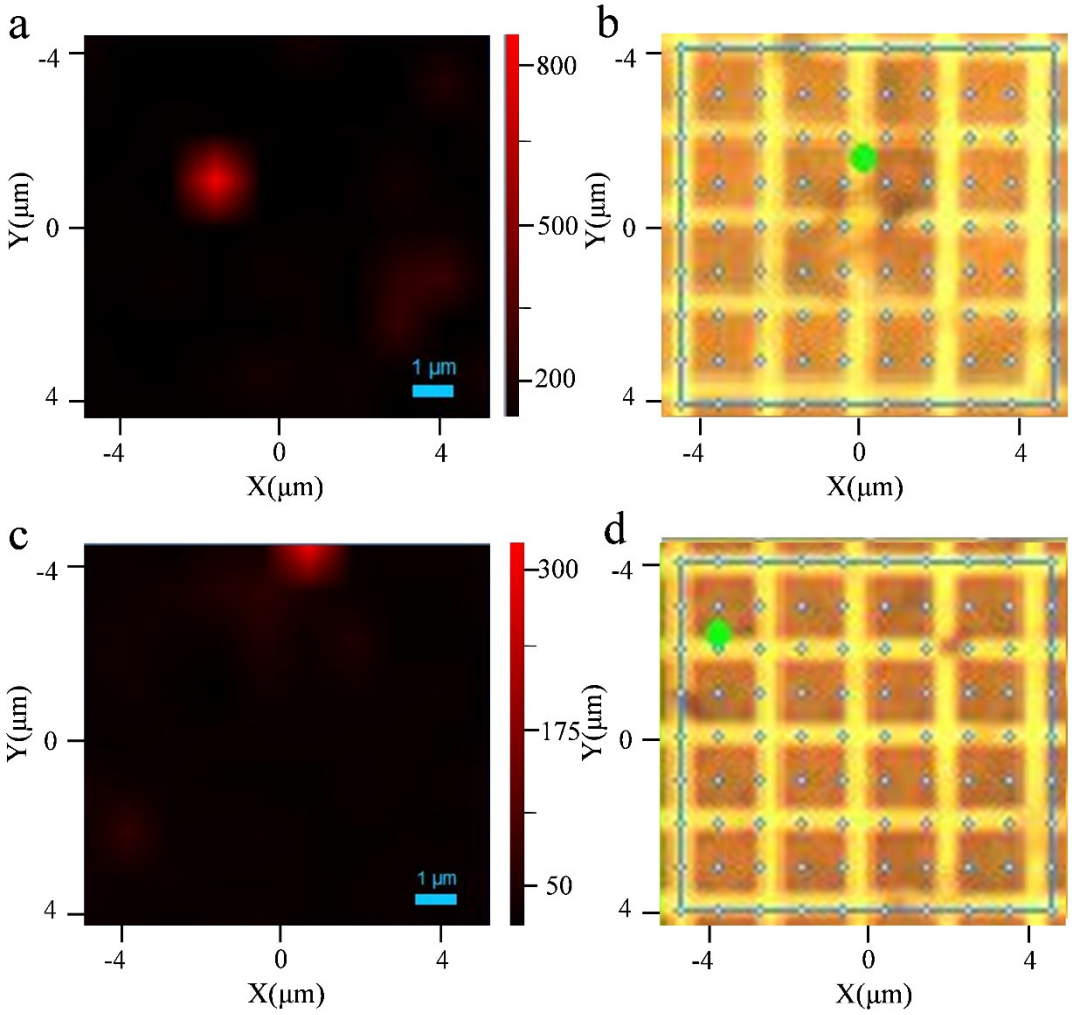

Figure 8. (a, b) Raman mapping image (a) and optical, bright field microscopic image (b) of polyethylene terephthalate (PET) particles on Klarite. (c, d) Raman mapping image (c) and microscopic image (d) of PS particles on Klarite. Scale bar: 2 µm. The green spot in b and d is the laser focus point while white spots are the sampling points.

Raman mapping was also employed to find the micro and nano plastics in ambient samples on Klarite (Figure 8). Point by point mapping of a regions approximately 9×8 μm^2, with the step size of 1 µm are presented. The peaks at 1003 cm^{-1} and 1617 cm^{-1} were used for mapping PS and PET respectively. As shown in Figure 8a and 8c, Raman mapping with SERS constitutes a facile and accurate means of determining distribution of micro- and nanoplastics on Klarite substrates, making subsequent analysis convenient. Despite the recent surge in

micro- and nanoplastics research worldwide, the detection and identification methods for such small particles is still challenging. The results presented here are encouraging and demonstrate the potential for SERS in this field of research.

4. ENVIRONMENTAL IMPLICATION

This paper demonstrates that SERS with Klarite is advantageous for identifying micro- and nanoplastics. The method is robust, facile and offsets the detection limit of microplastics by an order of magnitude, facilitating detection at the single nanoscale particle levels. PS and PMMA microplastics as small as 360 nm can clearly be identified via SERS, while standard Raman can barely detect particles as large as 5 μm. Here, SERS was also successfully applied to detect micro- and nanoplastics in ambient atmospheric aerosols. Together with numerical simulations, our experimental results show that enhancement factors from SERS are dependent not only on particle size, but also on particle location in the surface plasmon hotspots. Enhancement factors for PS were found to reach two orders of magnitude.

Although this paper demonstrates the potential for Klarite in the quantification of airborne microplastic pollution, further research is still required to overcome significant challenges. First, compared with lab generated samples, the Raman spectroscopic signal of atmospheric samples can be difficult to distinguish from the fluorescence background of unknown impurities. While approaches for increasing the concentration of microplastics are available, these approaches generally risk losing the smaller microplastics. Raman mapping combined with SERS offers a consolidation solution for detecting microplastics extracted from the atmosphere. Second, the Raman enhancement factor with Klarite appears to be variable for different analytes, and repeated cleaning and tests may cause certain damage to Klarite. One of the main challenges with SERS substrates is producing consistent and uniform hotpots of electric field enhancement. Despite the exceptional consistency and uniformity of Klarite substrates, further research is needed to improve the consistency and magnitude of the enhancement factors for different analytes. Third, even with Raman mapping techniques, quantitative analysis is still a challenge. It is anticipated that SERS could be combined with other microscopy and scanning probe techniques to facilitate both quantitative and qualitative of micro- and nanoplastics, as well as provide methodological support for studying the

impact of microplastics on human health.

SUPPORTING INFORMATION

SEM images and optical images of microplastics, photo of the setup, Raman spectra of PS and PMMA studied on different substrates (glass, Al foil). This material is available free of charge via the Internet at http://pubs.acs.org.

Author Information

Corresponding Author

E-mail: zhanglw@fudan.edu.cn

Phone/Fax: +86-21-6564-2781

Notes

The authors declare no competing financial interests.

Acknowledgements

The authors gratefully acknowledge financial support from the National Natural Science Foundation of China (No. 21976030 and No. 21677037), Ministry of Science and Technology of the People's Republic of China (2016YFE0112200 and 2016YFC0202700), the Natural Science Foundation of Shanghai (No. 19ZR1471200 and No. 17ZR1440200). VKV acknowledges support from the Royal Society through the University Research Fellowships and grants PEF1\170015 and RGF\EA\180228. VKV and RJ acknowledge the EPSRC iCASE studentships program.

References

1. Galgani, F.; Claro, F.; Depledge, M.; Fossi, C., Monitoring the impact of litter in large vertebrates in the Mediterranean Sea within the European Marine Strategy Framework Directive (MSFD): Constraints, specificities and recommendations. *Mar Environ Res* **2014,** *100*, 3-9.

2. Ding, J. F.; Jiang, F. H.; Li, J. X.; Wang, Z. X.; Sun, C. J.; Wang, Z. Y.; Fu, L.; Ding, N. X.; He, C. F., Microplastics in the Coral Reef Systems from Xisha Islands of South China Sea. *Environ. Sci. Technol.* **2019,** *53*, (14), 8036-8046.

3. Hu, L. L.; Chernick, M.; Hinton, D. E.; Shi, H. H., Microplastics in Small Waterbodies and Tadpoles from Yangtze River Delta, China. *Environ. Sci. Technol.* **2018,** *52*, (15), 8885-8893.

4. Schmidt, C.; Krauth, T.; Wagner, S., Export of Plastic Debris by Rivers into the Sea. *Environ. Sci. Technol.* **2017,** *51*, (21), 12246-12253.

5. Ravit, B.; Cooper, K.; Moreno, G.; Buckley, B.; Yang, I.; Deshpande, A.; Meola, S.; Jonesand, D.; Hsieh, A., Microplastics in urban New Jersey freshwaters: distribution, chemical identification, and biological affects. *Aims Environ Sci* **2017,** *4*, (6), 809-826.
6. Baldwin, A. K.; Corsi, S. R.; Mason, S. A., Plastic Debris in 29 Great Lakes Tributaries: Relations to Watershed Attributes and Hydrology. *Environ. Sci. Technol.* **2016,** *50*, (19), 10377-10385.
7. Dris, R.; Gasperi, J.; Rocher, V.; Saad, M.; Renault, N.; Tassin, B., Microplastic contamination in an urban area: a case study in Greater Paris. *Environ Chem* **2015,** *12*, (5), 592-599.
8. Li, W. C.; Tse, H. F.; Fok, L., Plastic waste in the marine environment: A review of sources, occurrence and effects. *Sci Total Environ* **2016,** *566*, 333-349.
9. Li, J. Y.; Liu, H. H.; Chen, J. P., Microplastics in freshwater systems: A review on occurrence, environmental effects, and methods for microplastics detection. *Water Res* **2018,** *137*, 362-374.
10. Zheng, Y. F.; Li, J. X.; Cao, W.; Liu, X. H.; Jiang, F. H.; Ding, J. F.; Yin, X. F.; Sun, C. J., Distribution characteristics of microplastics in the seawater and sediment: A case study in Jiaozhou Bay, China. *Sci Total Environ* **2019,** *674*, 27-35.
11. Song, Z. F.; Yang, X. Y.; Chen, F. M.; Zhao, F. Y.; Zhao, Y.; Ruan, L. L.; Wang, Y. G.; Yang, Y. S., Fate and transport of nanoplastics in complex natural aquifer media: Effect of particle size and surface functionalization. *Sci Total Environ* **2019,** *669*, 120-128.
12. Dris, R.; Gasperi, J.; Saad, M.; Mirande, C.; Tassin, B., Synthetic fibers in atmospheric fallout: A source of microplastics in the environment? *Mar Pollut Bull* **2016,** *104*, (1-2), 290-3.
13. Liu, K.; Wang, X. H.; Fang, T.; Xu, P.; Zhu, L. X.; Li, D. J., Source and potential risk assessment of suspended atmospheric microplastics in Shanghai. *Sci Total Environ* **2019,** *675*, 462-471.
14. Cai, L.; Wang, J.; Peng, J.; Tan, Z.; Zhan, Z.; Tan, X.; Chen, Q., Characteristic of microplastics in the atmospheric fallout from Dongguan city, China: preliminary research and first evidence. *Environ Sci Pollut Res Int* **2017,** *24*, (32), 24928-24935.
15. Klein, M.; Fischer, E. K., Microplastic abundance in atmospheric deposition within the Metropolitan area of Hamburg, Germany. *Sci Total Environ* **2019,** *685*, 96-103.
16. Allen, S.; Allen, D.; Phoenix, V. R.; Le Roux, G.; Jimenez, P. D.; Simonneau, A.; Binet, S.; Galop, D., Atmospheric transport and deposition of microplastics in a remote mountain catchment. *Nat Geosci* **2019,** *12*, (5), 339-+.
17. Dris, R.; Imhof, H.; Sanchez, W.; Gasperi, J.; Galgani, F.; Tassin, B.; Laforsch, C., Beyond the ocean: contamination of freshwater ecosystems with (micro-)plastic particles. *Environ Chem* **2015,** *12*, (5), 539-550.
18. Andrady, A. L., Microplastics in the marine environment. *Mar Pollut Bull* **2011,** *62*, (8), 1596-1605.
19. Jin, Y. X.; Xia, J. Z.; Pan, Z. H.; Yang, J. J.; Wang, W. C.; Fu, Z. W., Polystyrene microplastics induce microbiota dysbiosis and inflammation in the gut of adult zebrafish. *Environ Pollut* **2018,** *235*, 322-329.
20. Ahrendt, C.; Perez-Venegas, D. J.; Urbina, M.; Gonzalez, C.; Echeveste, P.; Aldana, M.; Pulgar, J.; Galban-Malagon, C., Microplastic ingestion cause intestinal lesions in the intertidal fish Girella laevifrons. *Mar Pollut Bull* **2020,** *151*.

21. Cox, K. D.; Covernton, G. A.; Davies, H. L.; Dower, J. F.; Juanes, F.; Dudas, S. E., Human Consumption of Microplastics. *Environ. Sci. Technol.* **2019,** *53*, (12), 7068-7074.
22. Phuong, N. N.; Zalouk-Vergnoux, A.; Kamari, A.; Mouneyrac, C.; Amiard, F.; Poirier, L.; Lagarde, F., Quantification and characterization of microplastics in blue mussels (Mytilus edulis): protocol setup and preliminary data on the contamination of the French Atlantic coast. *Environ Sci Pollut R* **2018,** *25*, (7), 6135-6144.
23. Rodriguez-Seijo, A.; Lourenco, J.; Rocha-Santos, T. A. P.; da Costa, J.; Duarte, A. C.; Vala, H.; Pereira, R., Histopathological and molecular effects of microplastics in Eisenia andrei Bouche. *Environ Pollut* **2017,** *220*, 495-503.
24. Setala, O.; Fleming-Lehtinen, V.; Lehtiniemi, M., Ingestion and transfer of microplastics in the planktonic food web. *Environ Pollut* **2014,** *185*, 77-83.
25. Wang, W. F.; Gao, H.; Jin, S. C.; Li, R. J.; Na, G. S., The ecotoxicological effects of microplastics on aquatic food web, from primary producer to human: A review. *Ecotox Environ Safe* **2019,** *173*, 110-117.
26. Mercogliano, R.; Avio, C. G.; Regoli, F.; Anastasio, A.; Colavita, G.; Santonicola, S., Occurrence of Microplastics in Commercial Seafood under the Perspective of the Human Food Chain. A Review. *J Agr Food Chem* **2020,** *68*, (19), 5296-5301.
27. Zhang, F.; Wang, X. H.; Xu, J. Y.; Zhu, L. X.; Peng, G. Y.; Xu, P.; Li, D. J., Food-web transfer of microplastics between wild caught fish and crustaceans in East China Sea. *Mar Pollut Bull* **2019,** *146*, 173-182.
28. Walczak, A. P.; Hendriksen, P. J. M.; Woutersen, R. A.; van der Zande, M.; Undas, A. K.; Helsdingen, R.; van den Berg, H. H. J.; Rietjens, I. M. C. M.; Bouwmeester, H., Bioavailability and biodistribution of differently charged polystyrene nanoparticles upon oral exposure in rats. *J Nanopart Res* **2015,** *17*, (5).
29. Ma, Y. N.; Huang, A. N.; Cao, S. Q.; Sun, F. F.; Wang, L. H.; Guo, H. Y.; Ji, R., Effects of nanoplastics and microplastics on toxicity, bioaccumulation, and environmental fate of phenanthrene in fresh water. *Environ Pollut* **2016,** *219*, 166-173.
30. Rodrigues, M. O.; Abrantes, N.; Goncalves, F. J. M.; Nogueira, H.; Marques, J. C.; Goncalves, A. M. M., Impacts of plastic products used in daily life on the environment and human health: What is known? *Environ Toxicol Phar* **2019,** *72*.
31. Vethaak, A. D.; Leslie, H. A., Plastic Debris Is a Human Health Issue. *Environ. Sci. Technol.* **2016,** *50*, (13), 6825-6826.
32. Wright, S. L.; Kelly, F. J., Plastic and Human Health: A Micro Issue? *Environ. Sci. Technol.* **2017,** *51*, (12), 6634-6647.
33. Gard, E.; Mayer, J. E.; Morrical, B. D.; Dienes, T.; Fergenson, D. P.; Prather, K. A., Real-time analysis of individual atmospheric aerosol particles: Design and performance of a portable ATOFMS. *Analytical Chemistry* **1997,** *69*, (20), 4083-4091.
34. Li, W. J.; Shao, L. Y.; Zhang, D. Z.; Ro, C. U.; Hu, M.; Bi, X. H.; Geng, H.; Matsuki, A.; Niu, H. Y.; Chen, J. M., A review of single aerosol particle studies in the atmosphere of East Asia: morphology, mixing state, source, and heterogeneous reactions. *J Clean Prod* **2016,** *112*, 1330-1349.
35. Posfai, M.; Xu, H. F.; Anderson, J. R.; Buseck, P. R., Wet and dry sizes of atmospheric aerosol particles: An AFM-TEM study. *Geophys Res Lett* **1998,** *25*, (11), 1907-1910.
36. Suaria, G.; Avio, C. G.; Mineo, A.; Lattin, G. L.; Magaldi, M. G.; Belmonte, G.; Moore, C.

J.; Regoli, F.; Aliani, S., The Mediterranean Plastic Soup: synthetic polymers in Mediterranean surface waters. *Sci Rep-Uk* **2016,** *6*.
37. Kappler, A.; Fischer, D.; Oberbeckmann, S.; Schernewski, G.; Labrenz, M.; Eichhorn, K. J.; Voit, B., Analysis of environmental microplastics by vibrational microspectroscopy: FTIR, Raman or both? *Anal Bioanal Chem* **2016,** *408*, (29), 8377-8391.
38. Pivokonsky, M.; Cermakova, L.; Novotna, K.; Peer, P.; Cajthaml, T.; Janda, V., Occurrence of microplastics in raw and treated drinking water. *Sci Total Environ* **2018,** *643*, 1644-1651.
39. Cabernard, L.; Roscher, L.; Lorenz, C.; Gerdts, G.; Primpke, S., Comparison of Raman and Fourier Transform Infrared Spectroscopy for the Quantification of Microplastics in the Aquatic Environment. *Environ. Sci. Technol.* **2018,** *52*, (22), 13279-13288.
40. Moller, J. N.; Loder, M. G. J.; Laforsch, C., Finding Microplastics in Soils: A Review of Analytical Methods. *Environ. Sci. Technol.* **2020,** *54*, (4), 2078-2090.
41. Wright, S. L.; Levermore, J. M.; Kelly, F. J., Raman Spectral Imaging for the Detection of Inhalable Microplastics in Ambient Particulate Matter Samples. *Environ. Sci. Technol.* **2019,** *53*, (15), 8947-8956.
42. Zhu, X.; Nguyen, B.; You, J. B.; Karakolis, E.; Sinton, D.; Rochman, C., Identification of Microfibers in the Environment Using Multiple Lines of Evidence. *Environ. Sci. Technol.* **2019,** *53*, (20), 11877-11887.
43. Gillibert, R.; Balakrishnan, G.; Deshoules, Q.; Tardivel, M.; Magazzu, A.; Donato, M. G.; Marago, O. M.; Lamy de La Chapelle, M.; Colas, F.; Lagarde, F.; Gucciardi, P. G., Raman Tweezers for Small Microplastics and Nanoplastics Identification in Seawater. *Environ. Sci. Technol.* **2019,** *53*, (15), 9003-9013.
44. Fu, Y.; Kuppe, C.; Valev, V. K.; Fu, H.; Zhang, L.; Chen, J., Surface-Enhanced Raman Spectroscopy: A Facile and Rapid Method for the Chemical Component Study of Individual Atmospheric Aerosol. *Environ. Sci. Technol.* **2017,** *51*, (11), 6260-6267.
45. Jones, R. R.; Hooper, D. C.; Zhang, L. W.; Wolverson, D.; Valev, V. K., Raman Techniques: Fundamentals and Frontiers. *Nanoscale Res Lett* **2019,** *14*.
46. Slade, J. H.; Ault, A. P.; Bui, A. T.; Ditto, J. C.; Lei, Z.; Bondy, A. L.; Olson, N. E.; Cook, R. D.; Desrochers, S. J.; Harvey, R. M.; Erickson, M. H.; Wallace, H. W.; Alvarez, S. L.; Flynn, J. H.; Boor, B. E.; Petrucci, G. A.; Gentner, D. R.; Griffin, R. J.; Shepson, P. B., Bouncier Particles at Night: Biogenic Secondary Organic Aerosol Chemistry and Sulfate Drive Diel Variations in the Aerosol Phase in a Mixed Forest. *Environ. Sci. Technol.* **2019,** *53*, (9), 4977-4987.
47. Wang, W. F.; Ndungu, A. W.; Li, Z.; Wang, J., Microplastics pollution in inland freshwaters of China: A case study in urban surface waters of Wuhan, China. *Sci Total Environ* **2017,** *575*, 1369-1374.
48. Pilot, R.; Signorini, R.; Durante, C.; Orian, L.; Bhamidipati, M.; Fabris, L., A Review on Surface-Enhanced Raman Scattering. *Biosensors-Basel* **2019,** *9*, (2).
49. Parker, J. H.; Feldman, D. W.; Ashkin, M., Raman Scattering by Silicon and Germanium. *Phys Rev* **1967,** *155*, (3), 712-&.
50. Tahir, M. A.; Zhang, X.; Cheng, H.; Xu, D.; Feng, Y.; Sui, G.; Fu, H.; Valev, V. K.; Zhang, L.; Chen, J., Klarite as a label-free SERS-based assay: a promising approach for atmospheric bioaerosol detection. *Analyst* **2019,** *145*, (1), 277-285.
51. Vernon, K. C.; Davis, T. J.; Scholes, F. H.; Gomez, D. E.; Lau, D., Physical mechanisms

behind the SERS enhancement of pyramidal pit substrates. *J Raman Spectrosc* **2010,** *41*, (10), 1106-1111.

52. Heller, E. J.; Yang, Y.; Kocia, L.; Chen, W.; Fang, S. A.; Borunda, M.; Kaxiras, E., Theory of Graphene Raman Scattering. *Acs Nano* **2016,** *10*, (2), 2803-2818.

591

592 **TOC**

593

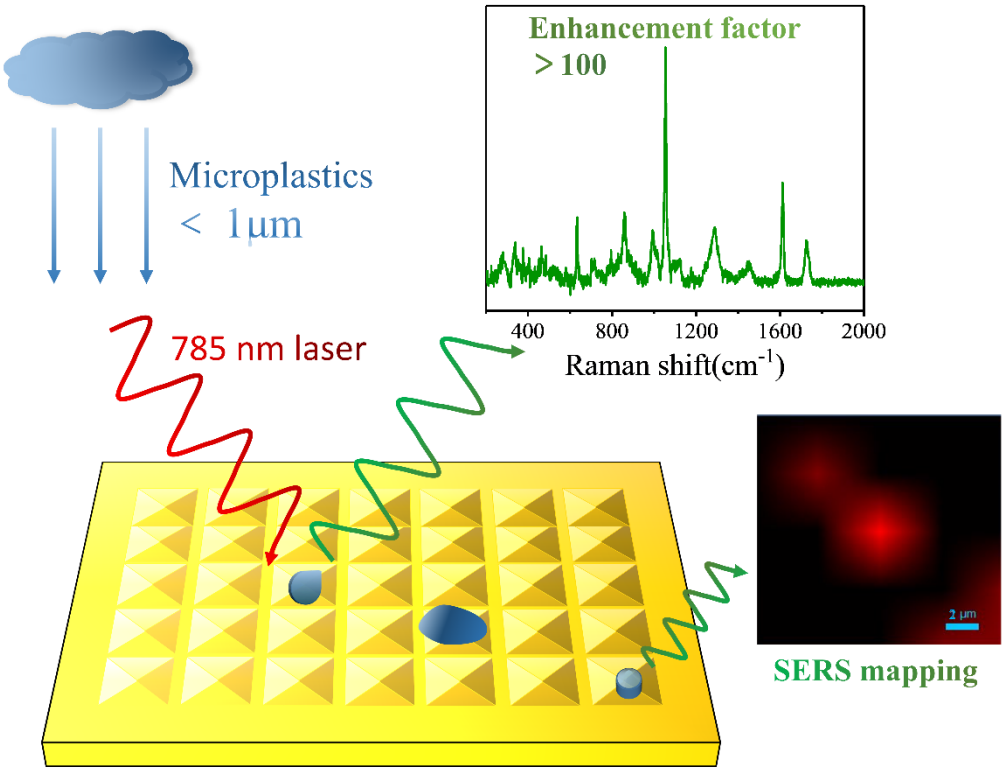

594